Case Studies in Thermal Engineering 72 (2025) 106427

Contents lists available at ScienceDirect

Case Studies in Thermal Engineering

journal homepage: www.elsevier.com/locate/csite

A neural network-based programming paradigm for heat transport of Eyring-Powell fluid with physiological blood flow applications

Abaker A. Hassaballa [a,f], Ali Imran [b], Ines Hilali Jaghdam [c], Jongsuk Ro [d,e,*]

[a] Center for Scientific Research and Entrepreneurship, Northern Border University, Arar 73213, Saudi Arabia
[b] Department of Mathematics, COMSATS University Islamabad, Attock Campus, Kamra Road Attock, Pakistan
[c] Department of Computer Science and Information Technology, Applied College, Princess Nourah bint Abdulrahman University, P.O. Box 84428, Riyadh 11671, Saudi Arabia
[d] School of Electrical and Electronics Engineering, Chung-Ang University, Dongjak-gu, Seoul, 06974, Republic of Korea
[e] Department of Intelligent Energy and Industry, Chung-Ang University, Dongjak-gu, Seoul, 06974, Republic of Korea
[f] Department of Mathematics, Faculty of Science, Northern Border University, Arar, 73213, Saudi Arabia

ARTICLE INFO

Keywords:
Eyring powell fluid
Complex cilia wave
Thermal slip
bvp5c technique
Levenberg-marquardt back propagation
Stability analysis

ABSTRACT

Complex cilia waves have diverse applications in physiological flow transport across various biological systems. This study presents a novel investigation into the effects of electroosmosis in a non-uniform channel lined with cilia for an Eyring-Powell model fluid. The objective is to examine how fluid transport is influenced in a non-uniform microchannel. Fluid transport characteristics are analyzed within a micro-ciliated channel by applying velocity and thermal slip boundary conditions under the influence of an electric field. Biological fluid flow is modeled using the relevant equations of motion, which are further simplified through low Reynolds number and long wavelength approximations. The physical fluid flow is solved using the bvp5c technique in MATLAB, and the computational scheme's validity is confirmed through artificial neural network (ANN) modeling. Stability analysis is conducted on the bvp5c solution, which is essential for verifying the numerical solution of the boundary value problem. A significant increase in biological fluid transport is observed with the slip parameter, while flow is suppressed by the Helmholtz-Smoluchowski velocity parameter. The temperature of fluid particles increases with the Brinkman number, thermal slip, and electroosmotic parameter but decreases with the thermal conductivity parameter and the Helmholtz-Smoluchowski velocity parameter. Diffusion phenomena are enhanced by the thermal conductivity and Helmholtz-Smoluchowski velocity parameters but are reduced by the concentration slip parameter and electroosmosis. The findings of this investigation may be instrumental in understanding blood transport in small arteries and developing treatments for dysfunctions in such systems.

Nomenclature

Symbol	Description	Symbol	Description
A	Eyring-Powell fluid material parameter	Uhs	Helmholtz-Smoluchowski velocity
B	Eyring-Powell fluid material parameter	$\hat{V}$	Transverse velocity component

(*continued on next page*)

* Corresponding author. School of Electrical and Electronics Engineering, Chung-Ang University, Dongjak-gu, Seoul, 06974, Republic of Korea.
E-mail addresses: Abaker.abdalla@nbu.edu.sa (A.A. Hassaballa), aimran_32029@yahoo.com (A. Imran), Imalihilali@pnu.edu.sa (I. Hilali Jaghdam), jsro@cau.ac.kr (J. Ro).

https://doi.org/10.1016/j.csite.2025.106427
Received 19 February 2025; Received in revised form 16 April 2025; Accepted 27 May 2025
Available online 1 June 2025

(*continued*)

Br	Brinkman number	$\widehat{X}$	Axial coordinate
$\widehat{C}$	Concentration	$\widehat{X}_0$	Reference axial position of fluid element
C_0	Reference concentration	$\widehat{Y}$	Transverse coordinate
D	Mass diffusivity	a	Expressing non-uniformity of the microchannel
E_0	Electric field strength	a_0	Mean half breadth at the inlet
E	Electric parameter	a_1	Mean half measurement of the outlet
Ec	Eckert number	c	Cilia wave speed
F	Flow rate	c_p	Specific heat at constant pressure
G	Axial position of cilia tip	e	Elementary charge
$\widehat{H}$	Channel height	h	Non-dimensional channel height H/a_0
K	Thermal conductivity function	k	Electroosmotic parameter/Thermal conductivity function
K_T	Thermal diffusion ratio	k_1	Thermal conductivity constant
$\widehat{P}$	Pressure	n_0	Ion concentration
Pr	Prandtl number	p	Non-dimensional pressure
Re	Reynolds number	$\widehat{t}$	Time
Sc	Schmidt number	$\widehat{u}$	Axial velocity in wave frame
Sr	Soret number	$\widehat{v}$	Transverse velocity in wave frame
$\widehat{T}$	Temperature	$\widehat{x}$	Axial coordinate in wave frame
T_0	Reference temperature	x	Non-dimensional axial coordinate
T_1	Wall temperature	$\widehat{y}$	Transverse coordinate in wave frame
$\widehat{U}$	Axial velocity component	y	Non-dimensional transverse coordinate
z	Valence of ion		
Greek Letter			
Θ	Non-dimensional temperature	μ	Dynamic viscosity (non-dimensional)
Φ	Electrical potential (non-dimensional)	μ_0	Reference dynamic viscosity
α	Eccentricity of ciliary motion	ρ	Density
α_1	Variable viscosity parameter	ρ_e	Charge density
α_2	Thermal conductivity variation parameter	$\widehat{\tau}_{ij}$	Stress components (dimensional)
β_1	Slip parameter at	τ_{ij}	Stress components (non-dimensional)
β_2	Thermal slip parameter	ψ	Stream function
β_3	Concentration slip parameter	$\widehat{\phi}$	Electric potential dimensional
δ	Amplitude ratio	ϵ	Permittivity of medium
ε_1	Amplitude of wave	ϵ_0	Permittivity of free space
ε_2	Amplitude of wave	λ_D	Debye length
λ	Wavelength of cilia wave		

1. Introduction

The dynamics of cilia have immense significance in investigating biological fluid transport, especially in the human body. Cilia is plural of Cilium having dimensions $10\mu m$ length and $0.25\mu m$ in breadth. Cilia are found on the free surface of eukaryotic cells. Synchronized passage of cilia is responsible for transport of fluid in various physiological settings. Mechanisms of cilia play pivotal role in physical phenomena like locomotion, alimentation, circulation, respiration, and reproduction [1]. Cilia are grouped into motile and immotile cilia, motile cilia are found in unicellular and multicellular physiological mechanism to transport the fluid or transport the fluid across them. Ciliary motility is induced by microtubule-based molecular compilation recognized as axoneme. Cilia perform various tasks in human body for instance, the continuous cleansing of lungs is done cilia beating waves [2,3]. In various microorganisms like paramecium, synchronized beating of cilia provide help in excellent locomotion [4]. The complex nature of ciliary beating and their mutual interaction within a physiological environment makes it difficult to understand the developing wave features, despite of the fact that many theoretical and experimental investigations have been reported. Various models to comprehend the ciliary wave patterns are reported [5–9], to investigate the conditions needed for coordinated movement and physical parameters that administer the properties of the metachronal wave in the mucus transport. The interaction of cilia [10,11] with the flow field produced their beats and emerging characteristics of the metachronal wave with the geometrical arrangement of the cilia, for instance cilia spacing and beat direction. Asghar et al. [12] presented the theoretical study for Newtonian fluid induce by metachronal waves within a permeable curved channel. Fluid transport induced by electroosmosis in a microtube [13,14], within ciliated microchannel, by implementing Joule heating and thermal radiation are reported. Novel features using Williamson fluid transport with heat transfer effects in a micro ciliated channel are reported by Imran et al. [15]. Shear-reliant peristaltic transport of rheological fluid inside the ciliated micro-channel investigated [16–18] with the aid of numerical simulations. The biomechanics of cilia-induce transport of Jeffrey nanofluid within a curved microchannel [19–21] and used shooting technique to gather the solution for velocity, temperature, and nanoparticle concentration profiles.

The electrokinetics-oriented pumping scheme has a widespread application in microscale transport, medical sciences, bioengineering, medical procedure monitoring, and beyond its adaptable abilities. Electro-pumping paradigm [22–24] of rheological nanofluid in the ciliated by taking various fluid flow axioms like entropy generation are reported in the literature.

Ciliary transport with heat and mass transport are important with heat convection from blood flow using tissue pores and heat transfer within tissues. Balance of temperature within the body is one of the basic functions of the human circulatory organism. The heats transfer is really instrumental while investigating the flow attributes. Cilia induced heat transfer has widespread utilities, for instance evaporation on the water body in energy transmission, in wet chilling Towers, in and drying processes.

Ellahi et al., [25] investigated the impacts of various flow parameters for two- and three-dimensional flow and reported that that wall shear stress is significantly reduced with shear thinning. Akram et al., [26] determined the peristaltic flow of Bingham fluid with MHD in wavy channel coupled with the effects of heat and mass communication. Electromagnetohydrodynamic oriented transport [27,28] for gold-blood nanofluid in asymmetric ciliated microchannel investigated with the aid numerical simulations.

By slip conditions means that the velocity of fluid is different relevant to the boundary and fluid layer adjacent to the boundary may slip. There are various natural systems that may be employed to examine the development of slip. The slip conditions appear at the boundary where the shear induced flow is introduced for biological fluid. The consequence of slip boundary conditions investigated [29] for the transport of Newtonian and Maxwellian fluid within permeable axisymmetric cylindrical tube with peristaltic motion. The variations of velocity slip, thermal slip and concentration slip for electrically conducted nanofluid for peristaltic flow are investigated [30,31] using a numerical technique. Rheological fluids transport over magnetized porous surface were reported [32–34], by implementing velocity and temperature slip, heat generation, and chemical reactions. Employed Lie symmetry assessment and the shooting method, the governing equations were tackled, and an AI-based neural network. Authors have shown that mass transfer increases with Schmidt number and chemical reaction rate, with higher concentration observed for non-porous surfaces.

The Eyring-Powell model [35] covers key flow axioms comprised of complex mathematical representation having viscous and elastic characteristics. The Eyring Powell fluid model having diverse physical significance has gathered the attention of many contemporary researchers. Heat and diffusion phenomenon relying on Eyring-Powell fluid investigated [36]. Gudekote et al. [37] investigated the peristaltically induced transport of Eyring Powell fluid within a non-uniform channel under the influence of varying fluid properties. The effect of Electroosmosis for Eyring-Powell model fluid in non-uniform are investigated [38] with varying wall properties by implementing the convective boundary conditions and gathered the solution using perturbation technique. The rheological transport properties are explored [39–41] for electrically conducting Casson nanofluid model for system of coupled partial differential equations by employing perturbation approach and explained the consequence of the Ohmic heating and viscous dissipation through a vertical permeable channel.

Focusing on the significance of nanofluid peristaltic applications, various studies are reported [42–44] to investigate the convective rheological nanofluid flow within a transversely divergent channel and highlight key fluidic phenomena such as viscous and Ohmic dissipation, energy generation, and activation energy. Neural network-based investigations were reported [45–47] for fluid transport over a flat surface with suction/injection and heat-mass transfer effects. Lie symmetry along with the shooting method were exploited to explain the reduced system, with a neural model predicting the Nusselt number based on key parameters. Consequences of their investigations showed that the Nusselt number increases with the temperature power law index, Prandtl number, and suction, but decreases with the PE fluid parameter.

The motivation for using the Eyring-Powell fluid model lies in its ability to accurately capture the rheological behavior of many real-world physiological fluids. Unlike simple Newtonian models, the Eyring-Powell model accounts for both shear-thinning and shear-thickening properties. Thus, when studying physiological flows, particularly under ciliary activity, where the fluid is moved in very delicate and varying shear environments, the Eyring-Powell model provides a more realistic and reliable representation of the fluid's behavior. A thorough study of the literature reveals that consequences of electroosmosis, slip boundary conditions, rheological fluid, in the context of blood flow for complex cilia motion has not gathered much attention. So, keeping in view the above narrated key fluid properties induced by complex cilia wave for the Eyring-Powell model by implanting slip at the boundaries with the variable thermal properties and electric field. In this investigation biological fluid transport is modeled using the governing equations of motion and simplified through low Reynolds number and long wavelength approximations. The solution is attained using bvp5c technique in MATLAB, and the computational scheme's validity is confirmed through ANN modeling. Stability analysis is conducted on the bvp5c solution, which is essential for verifying the numerical computations of the boundary value problem.

1.1. Flow design for rheological fluid

A two-dimensional complex cilia transport flow of the Eyring-Powell model is focused. The transport of rheological fluid is managed in an approach that the complex cilia wave travel along $\widehat{X}$-axis and $\widehat{Y}$-axis is transverse to it. The fluid transport characteristics are interrogated within a non-uniform micro ciliated microchannel by implementing velocity and thermal slip boundary conditions under the influence of an electric field.

The mathematical expression for the boundaries of non-uniform micro-channel [12,48,49] is

$$\widehat{H}(\widehat{X},t)=a(\widehat{X})+b\left(\epsilon_1\cos\left(\frac{2\pi}{\lambda}(\widehat{X}-c\widehat{t})\right)+\epsilon_2\cos\left(\frac{4\pi}{\lambda}(\widehat{X}-c\widehat{t})\right)\right), \tag{1}$$

Where $a(\widehat{X})=a_0+a_1\widehat{X}$, c interprets cilia wave speed, a expressing non-uniformity of the microchannel, λ is wavelength, $\widehat{t}$ is the time, a_0 mean half breadth at the inlet, and a_1 mean half measurement of the outlet, ϵ_1, ϵ_2 expressing amplitudes of the wave.

The dynamics of cilia tips in the axial direction may be described as:

$$G(\widehat{X},\widehat{X}_0,\widehat{t})=\widehat{X}_0+a\alpha\left(\varepsilon_1\cos\left(\frac{2\pi}{\lambda}(\widehat{X}-c\widehat{t})\right)+\varepsilon_2\cos\left(\frac{4\pi}{\lambda}(\widehat{X}-c\widehat{t})\right)\right), \tag{2}$$

$\widehat{X}_0$ corresponds to reference position of the rheological fluid, and α expressing eccentricity of ciliary motion. It has been concluded in many investigations that cilia adapt elliptic motion, and ciliary beat play decisive role in diverse physiological mechanisms. Complex cilia waves reduce to elementary cilia wave motion [1,49] when the parameters $\varepsilon_1 = \epsilon, \varepsilon_2 = 0$, and $\varepsilon_2 \neq 0, \varepsilon_1 \neq 0$ and $\varepsilon_1 + \varepsilon_2 \geq a$ are imperative conditions for the constitution of complex cilia wave. The physical fluid transport scheme within non-uniform ciliated channel is presented in Fig. 1(a).

The axial and transverse velocity components [12,48,49] at the boundary induced by complex cilia wave are:

$$\widehat{U}_0 = \frac{\frac{-2\pi a c\alpha}{\lambda}\left(\varepsilon_1 \cos\left(\frac{2\pi}{\lambda}(\widehat{X} - c\widehat{t})\right) + \varepsilon_1 \cos\left(\frac{4\pi}{\lambda}(\widehat{X} - c\widehat{t})\right)\right),}{1 - \frac{-2\pi a c\alpha}{\lambda}\left(\varepsilon_1 \cos\left(\frac{2\pi}{\lambda}(\widehat{X} - c\widehat{t})\right) + \varepsilon_1 \cos\left(\frac{4\pi}{\lambda}(\widehat{X} - c\widehat{t})\right)\right),}. \tag{3}$$

$$\widehat{V}_0 = \frac{\frac{-2\pi a c\alpha}{\lambda}\left(\varepsilon_1 \sin\left(\frac{2\pi}{\lambda}(\widehat{X} - c\widehat{t})\right) + \varepsilon_1 \sin\left(\frac{4\pi}{\lambda}(\widehat{X} - c\widehat{t})\right)\right),}{1 - \frac{-2\pi a c\alpha}{\lambda}\left(\varepsilon_1 \cos\left(\frac{2\pi}{\lambda}(\widehat{X} - c\widehat{t})\right) + \varepsilon_1 \cos\left(\frac{4\pi}{\lambda}(\widehat{X} - c\widehat{t})\right)\right),}. \tag{4}$$

The pertinent equations of fluid transport like conservation of mass, momentum and energy [37,38] are

$$\frac{\partial \widehat{U}}{\partial \widehat{X}} - \frac{\partial \widehat{V}}{\partial \widehat{Y}} = 0, \tag{5}$$

$$\rho\left(\frac{\partial}{\partial \widehat{t}} + \widehat{U}\frac{\partial}{\partial \widehat{X}} + \widehat{V}\frac{\partial}{\partial \widehat{Y}}\right)\widehat{U} = -\frac{\partial \widehat{p}}{\partial \widehat{X}} + \frac{\partial \widehat{\tau}_{\widehat{X}\widehat{X}}}{\partial \widehat{X}} + \frac{\partial \widehat{\tau}_{\widehat{X}\widehat{Y}}}{\partial \widehat{Y}} + \sigma_e E_0, \tag{6}$$

$$\rho\left(\frac{\partial}{\partial \widehat{t}} + \widehat{U}\frac{\partial}{\partial \widehat{X}} + \widehat{V}\frac{\partial}{\partial \widehat{Y}}\right)\widehat{V} = -\frac{\partial \widehat{p}}{\partial \widehat{Y}} + \frac{\partial \widehat{\tau}_{\widehat{Y}\widehat{X}}}{\partial \widehat{X}} + \frac{\partial \widehat{\tau}_{\widehat{Y}\widehat{Y}}}{\partial \widehat{Y}} \tag{8}$$

$$\rho C_p\left(\frac{\partial}{\partial \widehat{t}} + \widehat{U}\frac{\partial}{\partial \widehat{X}} + \widehat{V}\frac{\partial}{\partial \widehat{Y}}\right)\widehat{T} = k_1\left(\frac{\partial}{\partial \widehat{X}}\left(k(\widehat{T})\frac{\partial \widehat{T}}{\partial \widehat{X}}\right) + \frac{\partial}{\partial \widehat{Y}}\left(k(\widehat{T})\frac{\partial \widehat{T}}{\partial \widehat{Y}}\right)\right) +$$

$$+\widehat{\tau}_{\widehat{X}\widehat{X}}\frac{\partial \widehat{U}}{\partial \widehat{X}} + \widehat{\tau}_{\widehat{X}\widehat{Y}}\frac{\partial \widehat{V}}{\partial \widehat{X}} + \widehat{\tau}_{\widehat{X}\widehat{Y}}\left(\frac{\partial \widehat{U}}{\partial \widehat{X}} + \frac{\partial \widehat{V}}{\partial \widehat{Y}}\right) \tag{9}$$

$$\left(\frac{\partial \widehat{C}}{\partial \widehat{t}} + \widehat{U}\frac{\partial \widehat{C}}{\partial \widehat{X}} + \widehat{V}\frac{\partial \widehat{C}}{\partial \widehat{Y}}\right) = D\left(\frac{\partial^2 \widehat{C}}{\partial \widehat{X}^2} + \frac{\partial^2 \widehat{C}}{\partial \widehat{Y}^2}\right) + \frac{DK_T}{T_m}\left(\frac{\partial^2 \widehat{T}}{\partial \widehat{X}^2} + \frac{\partial^2 \widehat{T}}{\partial \widehat{Y}^2}\right) \tag{10}$$

$\widehat{U}, \widehat{V}$ signifies axial and transverse velocity components, $\widehat{\tau}_{\widehat{X}\widehat{X}}, \widehat{\tau}_{\widehat{X}\widehat{Y},}$ and $\widehat{\tau}_{\widehat{Y}\widehat{Y}}$ representing stress components, $\widehat{p}$ is the pressure, $\rho, k_1, \widehat{T}$ are density, mass diffusivity, and temperature respectively, C_p is the specific heat.

The Poisson equation [39] governing the *electric potential* ϕ for the *electric double layer* neighboring a charged surface is defined

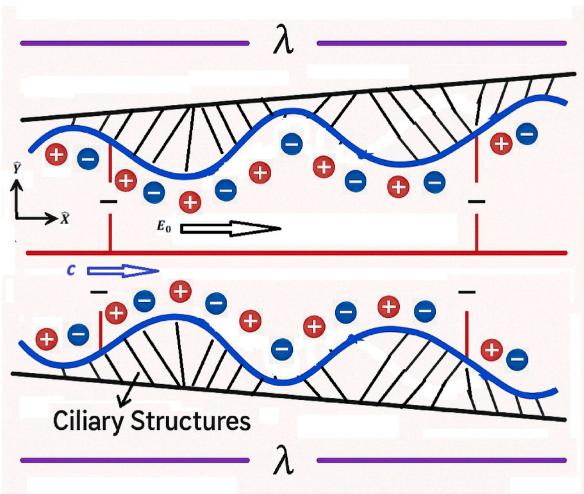

Fig. No. 1(a). Biological fluid transport scheme in non-uniform ciliated channel.

$$\frac{\partial^2 \widehat{\phi}}{\partial \widehat{Y}^2} = -\frac{\rho_e}{\widehat{\epsilon}}, \tag{12}$$

Where $\rho_e, \widehat{\epsilon}$ representing local charge density, and permittivity of the medium respectively. The charge density using Boltzman distribution is

$$\rho_e = -2zen_0 \sinh \frac{ze\widehat{\phi}}{T_* k_B}, \tag{13}$$

Where $z, n_0, e, k_B,$ and T_* expresses valence, ion concentration, elementary charge, Boltzman constant, and absolute temperature respectively. Implementing Eq. (12) into Eq. (11)

$$\frac{\partial^2 \widehat{\phi}}{\partial \widehat{Y}^2} = \frac{2zen_0}{\widehat{\epsilon}} \sinh \frac{ze\widehat{\phi}}{T_* k_B}, \tag{14}$$

Using the Debye–Hückel approximation $\sinh \frac{ze\widehat{\phi}}{T_* k_B} \approx \frac{ze\widehat{\phi}}{T_* k_B}$

$$\frac{\partial^2 \widehat{\phi}}{\partial \widehat{Y}^2} = k^2 \widehat{\phi}, \tag{15}$$

Where $k = \frac{2z^2 e^2 n_0}{\widehat{\epsilon}} \frac{1}{T_* k_B}$

The variable viscosity $\mu(y)$ and $K(\Theta)$ representing the thermal conductivity.

$$\mu(y) = 1 - \alpha_1 y, K(\Theta) = 1 + \alpha_2 \Theta \tag{16}$$

With $\alpha_1 \ll 1, \alpha_2 \ll 1$.

$$\widehat{u} + c = \widehat{U}, \widehat{x} = \widehat{X} - c\widehat{t}, \widehat{v} = \widehat{V}, \widehat{y} = \widehat{Y}, \widehat{p}(\widehat{x}, \widehat{y}) = \widehat{P}(\widehat{X}, \widehat{Y}, \widehat{t}). \tag{17}$$

Defining the non-dimensional parameters as

$$y = \frac{\widehat{y}}{a_0}, x = \frac{\widehat{x}}{\lambda}, v = \frac{\widehat{v}}{c\delta}, u = \frac{\widehat{u}}{c}, \delta = \frac{a_0}{\lambda}, p = \frac{\widehat{p} a_0^2}{\mu_0 c \lambda}, Re = \frac{c\rho_f a_0}{\mu_0}, h = \frac{\widehat{H}}{a_0}, \mu = \frac{\widehat{\mu}}{\mu_0},$$

$$\mathrm{k} = \frac{a_0}{\lambda_D}, \Theta = \frac{\widehat{T} - \widehat{T}_0}{\widehat{T}_0}, \gamma = \frac{\widehat{C} - \widehat{C}_0}{\widehat{C}_0}, Uhs = -\frac{E_x \epsilon \epsilon_0}{\mu c}, B_r = E_C\, Pr, Pr = \frac{C_p \mu}{k_0}, \tag{18}$$

$$E_c = \frac{c^2}{c_p(\widehat{T}_1 - \widehat{T}_0)}, Pr = \frac{c_p \mu_0}{k_0}, \tau_{ij} = \frac{a_0}{\mu c} \widehat{\tau}_{ij}, Sr = \frac{\rho D K_T (\widehat{T}_1 - \widehat{T}_0)}{T_m \widehat{C}_0}, Sc = \frac{\mu}{\rho D},$$

Where k, Uhs are is the electroosmotic and Helmholtz Smoluchowski velocity parameters, λ_D is the Debye length, Re is the Reynolds number, Br is the Brinkman number, Pr is the Prandtl number, Ec is the Eckert number, ϵ_0, ϵ is the permittivity of the free space and medium respectively

Now capitalizing the wave frame approximation, non-dimensional parameters and lubrication approximations, equations of motion take the shape

$$\frac{\partial^2 \phi}{\partial y^2} = k^2 \phi, \tag{19}$$

$$\frac{\partial p}{\partial x} = \frac{\partial}{\partial y} \left((\mu + B) \frac{\partial^2 \psi}{\partial y^2} - \frac{A}{3} \left(\frac{\partial^2 \psi}{\partial y^2} \right)^3 \right) + K^2 Uhs \Phi, \tag{20}$$

$$\frac{\partial p}{\partial y} = 0, \tag{21}$$

$$\frac{\partial}{\partial y} \left(k(\Theta) \frac{\partial \Theta}{\partial y} \right) + Br \left((\mu + B) \frac{\partial^2 \psi}{\partial y^2} - \frac{A}{3} \left(\frac{\partial^2 \psi}{\partial y^2} \right)^3 \right) \frac{\partial^2 \psi}{\partial y^2} = 0, \tag{22}$$

$$\frac{\partial^2 \gamma}{\partial y^2} + ScSr \frac{\partial^2 \Theta}{\partial y^2} = 0, \tag{23}$$

Eq. (21) infer that $p \neq p(y)$, and so $p = p(x)$ only

$$\frac{dp}{dx}=\frac{\partial^2}{\partial y^2}\left((\mu+B)\frac{\partial^2\psi}{\partial y^2}-\frac{A}{3}\left(\frac{\partial^2\psi}{\partial y^2}\right)^3\right)+k^2Uhs\Phi_y \tag{24}$$

Where A, B Eyring Powell fluid material parameters, Sc are, the Schmidth number, and Sr Soret number. The pertinent boundary conditions are

$\psi = F, \psi'' = 0, \Theta' = 0, \gamma' = 0, \phi[0] = 0,$ at $y = 0,$

$$\psi=0, \psi'+\beta_1\left[(1-\alpha_1 h+B)\psi''(h)-\frac{A}{3}(\psi''(h))^3\right]=u_0, at\, y=h \tag{25}$$

$\Theta + \beta_2\Theta' = 1, \gamma + \beta_3\gamma' = 1, \phi' = 1,$ at $y = h,$ Where $u_0 = (-1 + 2\pi\alpha\delta(\varepsilon_1 + \varepsilon_2)cos\, 2\,\pi x), h = 1 + mx + (\varepsilon_1 + \varepsilon_2)cos\, 2\,\pi x.$
Solving Eq. (19) w.r.t B. Cs (25) solution for Φ electrical potential may be obtained as

$$\Phi\frac{\mathrm{Sech}[hk]\mathrm{Sinh}[ky]}{k}. \tag{26}$$

1.2. The bvp5c scheme

The **bvp5c** is a wonderful computational technique for boundary value problems employed in MATLAB for tackling ordinary differential equations. This technique comprises collocation method with having a mesh refinement approach, established on a fifth-order precise algorithm. In this technique the solution is explored by estimating it with piecewise polynomials, adapting the mesh points iteratively to minimize error. This technique is really effective for problems having smooth solutions or minor singularities.

$$\psi=y(1), \psi'=y(2), \psi''=y(3), \psi'''=y(4), \Theta=y(5), \Theta'=y(6),$$

$$\gamma=y(7), \gamma'=y(8), dydx(1)=y(2), dydx(2)=y(3), dydx(3)=y(4)$$

By incorporating the above simplifications Eqs. 15–19 take the representations as:

$$dydx(4)=\frac{-k^2UhsCosh[ky]Sech[hk]+2\alpha_1 y(4)+2Ay(3)(y(4))^2}{1+B-\alpha_1 y-A(y(3))^2} \tag{27}$$

$$dydx(6)=\frac{-3\alpha_2 y(6)-3Br(y(3))^2-3BBr(y(3))^2+3\alpha_1 Bry(y(3))^2+ABr(y(3))^4}{3(1+\alpha_2 y)} \tag{28}$$

$$dydx(8)=-ScSrdydx(6) \tag{29}$$

And the respective boundary conditions are

$$y_a(1)-F, y_a(3)-0, y_a(6)-0, y_a(8)-0$$

$$y_b(1)-0, y_b(2)+\beta_1\left[(1-\alpha_1 h+B)y_b(3)-\frac{A}{3}(y_b(3))^3\right]-u_0, \tag{30}$$

$$y_b(5)+\beta_2 y_b(6)-1, y_b(7)+\beta_3 y_b(8)-1.$$

1.3. Artificial neural network

ANN is really effective computational technique evolved by organization and working of the human brain, constructed to distinguish models and solve complex problems. This scheme comprises of layers of connected nodes, or neurons, managed into an input layer, one or more hidden layers, and an output layer. Each relationship has a related weight, which is managed through training to minimize error using algorithms like backpropagation. ANNs has various applications, for instance image and speech identification, natural language processing, and predictive analytics by learning from data, recognizing relationships, and generalizing unseen scenarios. (Fig. 1(b and c)). The scheme of neural networks is illustrated in Fig. 1(c), figuring 5 inputs, 3 outputs, and a single hidden layer comprising 10 nodes. Individually link between the nodes is connected with a weight. The input layer is represented as $X = [x_1,$

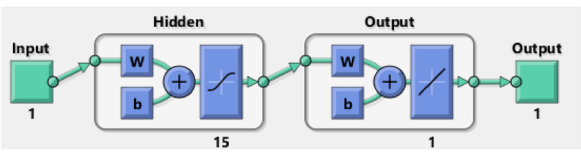

Fig. No. 1(b). Function fitting neural network.

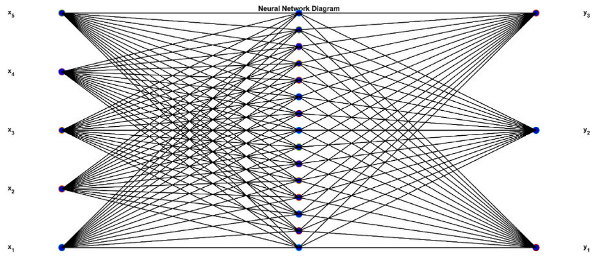

Fig. No. 1(c). Neural network diagram.

$x_2, \ldots, x_n]$ to the subsequent layer without any alterations. Each hidden layer is computed as

$$z_j^{(m)} = \sum_{i=1}^{n} w_{ij}^{(m)} a_i^{(m-1)} + b_j^{(m)}$$

$$a_i^{(m-1)} = f\left(z_j^{(m)}\right)$$

In the above equations m Layer index (for instance $m = 1, 2, \ldots$ for hidden layers), $\left(z_j^{(m)}\right.$: Weighted sum for the $j-th$ neuron in layer m, $w_{ij}^{(m)}$ refers to the weight joining neuron i in layer $m-1$ to neuron j in layer m, $b_j^{(m)}$ is Bias for the $j-th$ neuron in layer m, $a_i^{(m-1)}$ activation (output) from neuron i in layer $m-1$, $f\left(z_j^{(m)}\right)$ activation function.

The output layer functions identical to the hidden layer providing the predictions:

$$z_k^{(M)} = \sum_{j=1}^{k} w_{jk}^{(M)} a_j^{(M-1)} + b_k^{(M)}$$

$$y_k = g\left(z_k^{(M)}\right)$$

In the above provided equations L final output layer, $\left.z_k^{(M)}\right)$ representing weighted sum, $z_k^{(M)}$ activation function pertaining to the task, y_k expressing output function.

2. Result discussion on the resultant outcomes

A novel investigation for revealing the effect of electroosmotic in a non-uniform channel carpeted with cilia for Eyring-Powell model fluid is studied. How the fluid transport is affected in non-uniform is the main objective of this study. The fluid transport characteristics are interrogated within a micro ciliated microchannel by implementing velocity and thermal slip boundary conditions under the influence of an electric field. Biological fluid flow is modeled using relevant equations of motion, which are further streamlined by implementing low Reynolds number and long wavelength approximations. Solution of the physical fluid flow is managed with bvp5c technique in MATLAB, authenticity of computation scheme is validated with ANN. Neural network scheme is shown in Fig. 1(b–c). In this juncture of investigation effects of various flow parameters like, material constants of Eyring fluid model, electroosmotic parameter, Helmholtz Smoluchowski velocity parameter, velocity, thermal, and concentration slip parameters etc. are interrogated.

Table 1
Show comparison of present study with Kizhakkumpatt et al. [35] by setting $\delta = 0, \varepsilon_1 = \varepsilon_2 = 0$

y	Present for $u(y)$	Kizhakkumpatt et al. [35]	Difference
0	− 0.55383400000000005	− 0.55046099999999998	0.0033730000000000001
0.111111	− 0.55193199999999998	− 0.54868099999999997	0.0032499999999999999
0.222222	− 0.54930000000000001	− 0.54641899999999999	0.0028809999999999999
0.33333299999999999	− 0.55070699999999995	− 0.54844300000000001	0.0022650000000000001
0.44444400000000001	− 0.56124799999999997	− 0.55984999999999996	0.0013990000000000001
0.55555600000000005	− 0.58651500000000001	− 0.58623400000000003	0.000281
0.66666700000000001	− 0.63280499999999995	− 0.63389799999999996	0.001093
0.77777799999999997	− 0.70740800000000004	− 0.71014299999999997	0.0027360000000000002
0.88888900000000004	− 0.81904200000000005	− 0.82371099999999997	0.0046690000000000004
1	− 0.97860899999999995	− 0.98554900000000001	0.00694

2.1. Convergence and comparison of bvp5c the solution

It has been observed in this study that bvp5c solver achieves convergence magnificently without warnings. The solution profiles are smooth, fulfilling boundary conditions with negligible residual errors. Squeezing solver tolerances and improving the mesh further confirms the convergence behavior. Therefore, the method is stable and reliable for the considered parameter ranges. The solution was

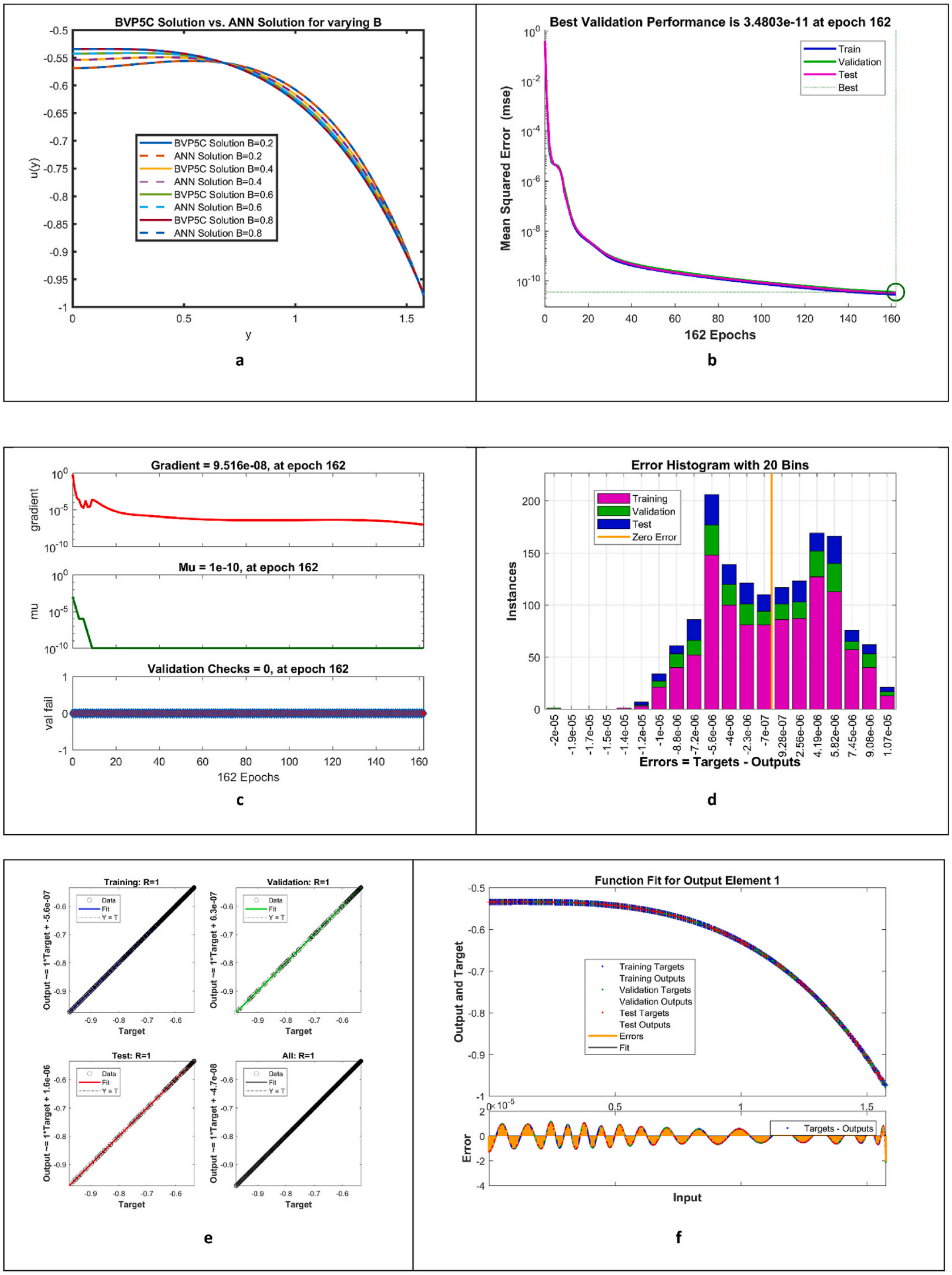

Fig. 2. Comprehensive analysis of BVP5C solution with ANN for varying material constant of Eyring-Powell model on velocity with $\boldsymbol{A} = 0.1, \boldsymbol{m} = 0.1, \boldsymbol{\alpha} = 0.2; \boldsymbol{\epsilon_1} = 0.3, \boldsymbol{\epsilon_2} = 0.4, \boldsymbol{\delta} = 0.01$; $\boldsymbol{F} = 2, \boldsymbol{x} = 0.1, \boldsymbol{k} = 1, \boldsymbol{\alpha_1} = 0.02, \boldsymbol{\alpha_2} = 0.02, \boldsymbol{\beta_1} = 0.01, \boldsymbol{\beta_2} = 0.01, \boldsymbol{\beta_3} = 0.01, \boldsymbol{Br} = 2, \boldsymbol{Sc} = 0.9, \boldsymbol{Sr} = 0.7, \boldsymbol{Uhs} = 3$.

obtained on a mesh of 1500 points. The maximum error is approximately 4.592×10^{-09}. There were nearly 52488 calls to the ODE function. There were 37 calls to the BC function. The Table 1 shows a comparison between the present study and Kizhakkumpatt et al. [38] for $\delta = 0, \varepsilon_1 = \varepsilon_2 = 0$. The present results for $u(y)$ closely match the reference values, with very small differences throughout the domain. The maximum observed difference is only about 0.00694, confirming excellent agreement between the two studies. Thus, the present study is successfully validated against the established results.

The flow chart for the numerical scheme is elaborated as:

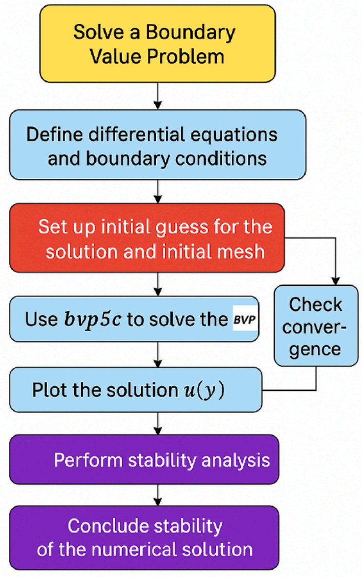

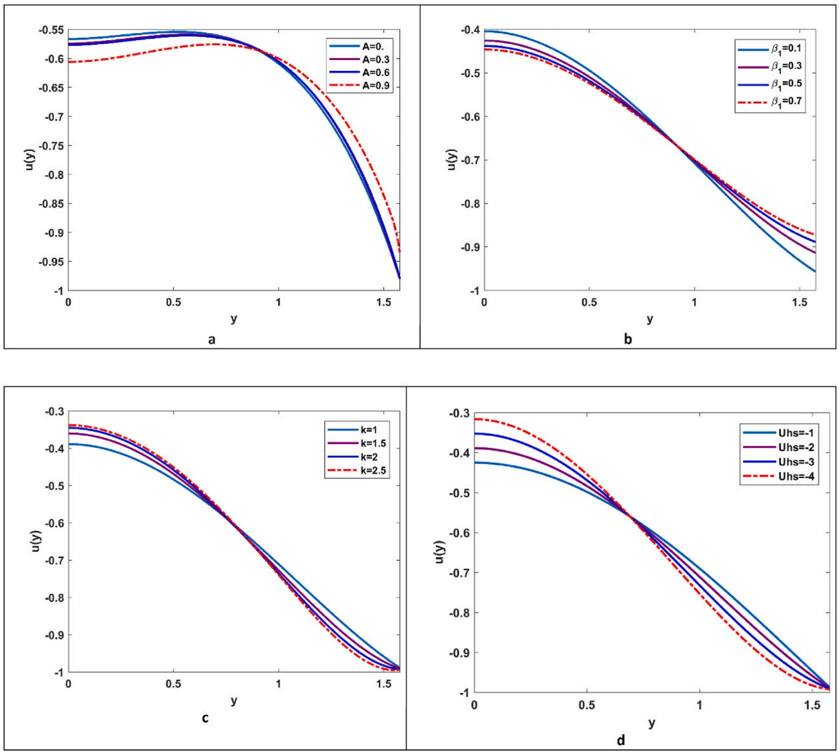

Fig. 3. Showcase the effect of Eyring Powell parameter, velocity slip, electroosmotic parameter, Helmholtz Smoluchowski velocity parameter on the velocity with B $= \mathbf{0.2}, \boldsymbol{m} = \mathbf{0.1}, \boldsymbol{\alpha} = \mathbf{0.2}; \boldsymbol{\epsilon_1} = \mathbf{0.3}, \boldsymbol{\epsilon_2} = \mathbf{0.4}, \boldsymbol{\delta} = \mathbf{0.01};\ \boldsymbol{F} = \mathbf{2}, \boldsymbol{x} = \mathbf{0.1}, \boldsymbol{k} = \mathbf{1}, \boldsymbol{\alpha_1} = \mathbf{0.02}, \boldsymbol{\alpha_2} = \mathbf{0.02}, \boldsymbol{\beta_1} = \mathbf{0.01}, \boldsymbol{\beta_2} = \mathbf{0.01}, \boldsymbol{\beta_3} = \mathbf{0.01}, \boldsymbol{Br} = \mathbf{2}, \boldsymbol{Sc} = \mathbf{0.9}, \boldsymbol{Sr} = \mathbf{0.7}, \boldsymbol{Uhs} = \mathbf{3}$.

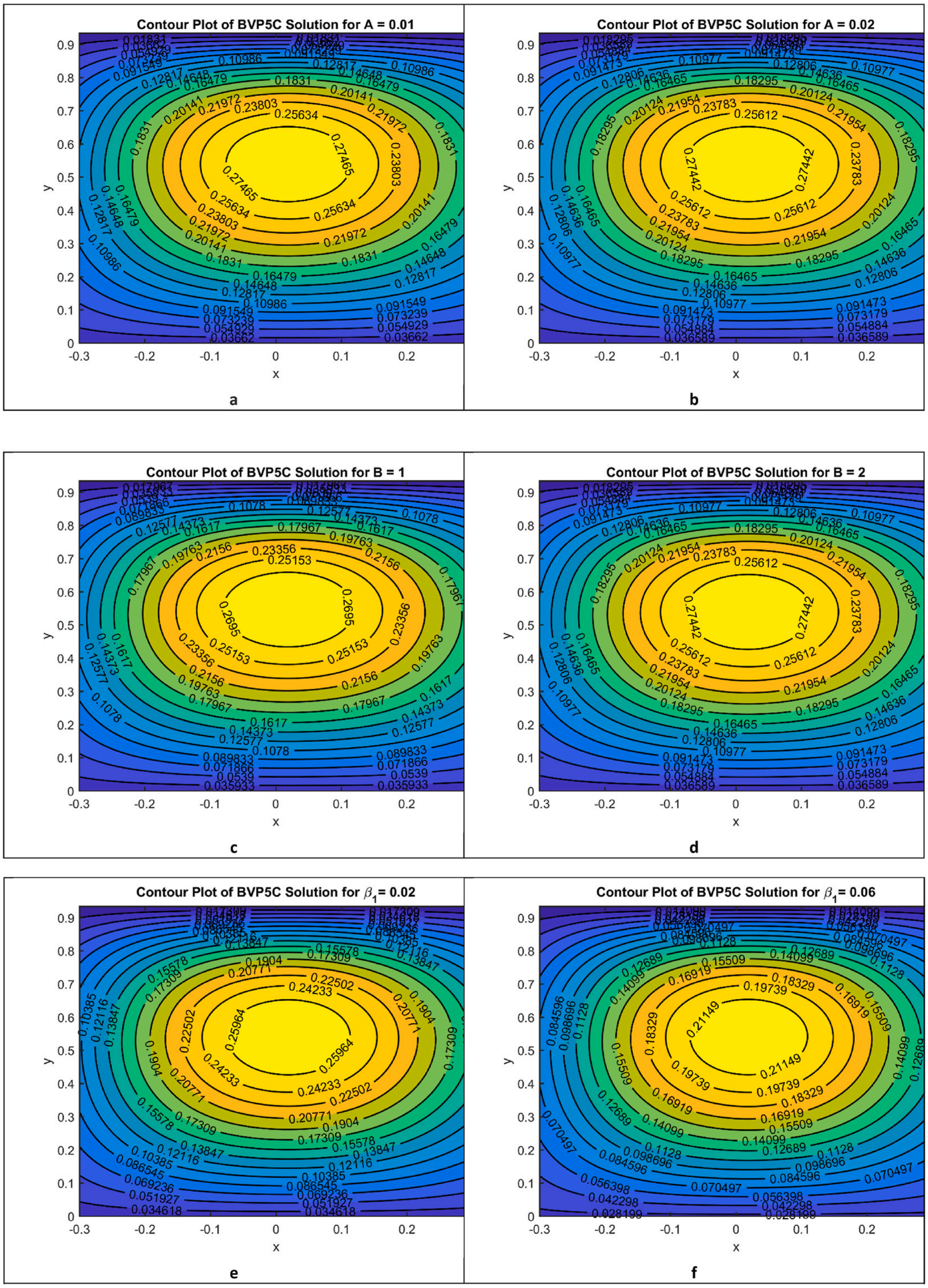

Fig. 4. Showing the effect of material constants of Eyring-Powell model, velocity slip parameter β_1, on the velocity distribution with $A = 0.1, B = 2, m = 0.1, \alpha = 0.2; \epsilon_1 = 0.3, \epsilon_2 = 0.4, \delta = 0.01;$ $F = 2, x = 0.1, k = 1, \alpha_1 = 0.02, \alpha_2 = 0.02, \beta_1 = 0.01, \beta_2 = 0.01, \beta_3 = 0.01, Br = 2, Sc = 0.9, Sr = 0.7, Uhs = 3.$.

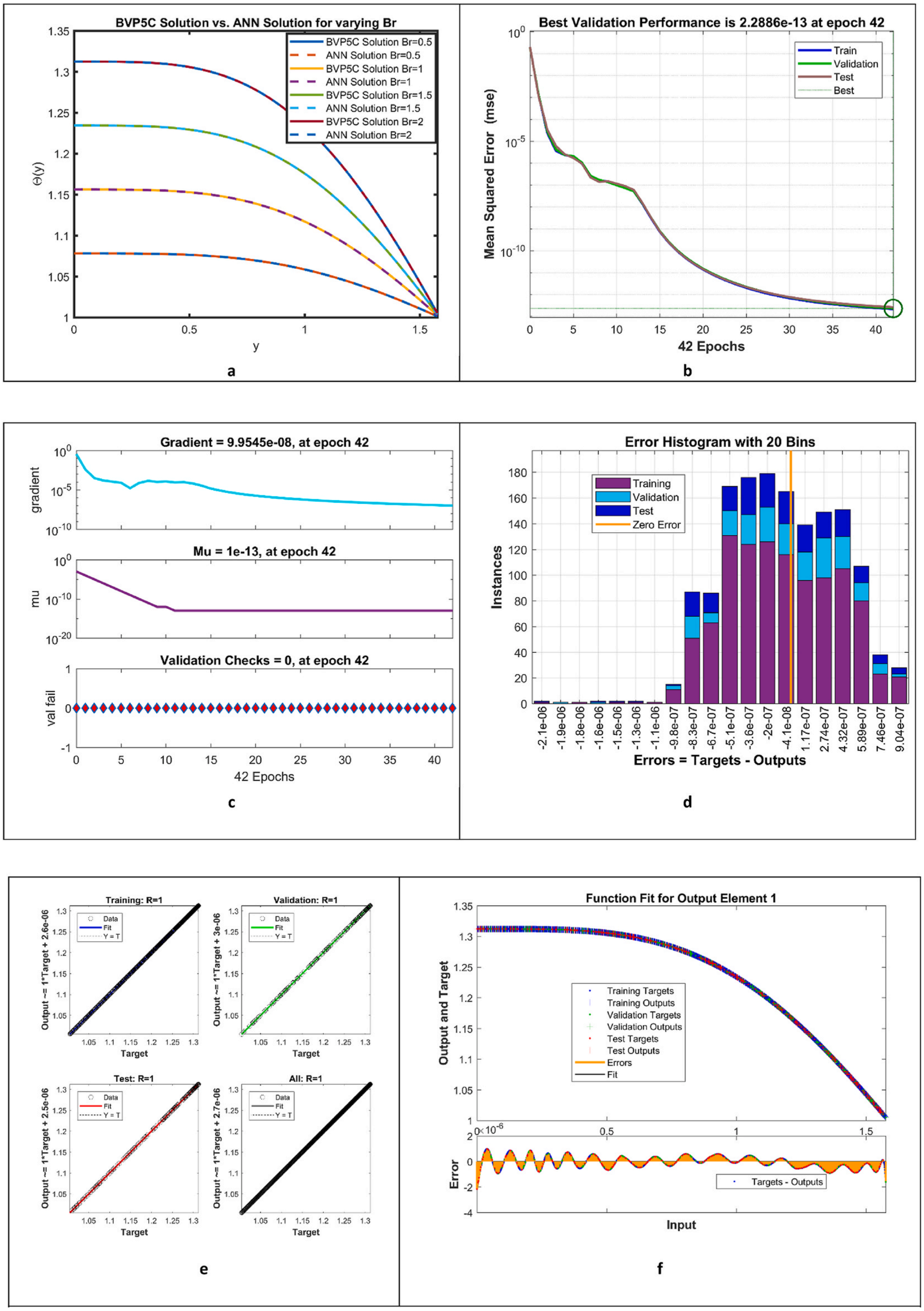

Fig. 5. Comparison of BVP5C with ANN solution for varying $\boldsymbol{Br}$ with $\boldsymbol{A} = 0.2, \boldsymbol{B} = 0.2, \boldsymbol{m} = 0.1, \boldsymbol{\alpha} = 0.2; \boldsymbol{\epsilon_1} = 0.3, \boldsymbol{\epsilon_2} = 0.4, \boldsymbol{\delta} = 0.01$; $\boldsymbol{F} = 2, \boldsymbol{x} = 0.1, \boldsymbol{k} = 1, \boldsymbol{\alpha_1} = 0.02, \boldsymbol{\alpha_2} = 0.02, \boldsymbol{\beta_1} = 0.01, \boldsymbol{\beta_2} = 0.01, \boldsymbol{\beta_3} = 0.01, \boldsymbol{Sc} = 0.9, \boldsymbol{Sr} = 0.7, \boldsymbol{Uhs} = 3$.

2.2. Velocity behavior

Fig. 2(a) showing the effect of Eyring Powell material constant B variations on the axial velocity profile with comparison with ANN. Absolute unanimity of bvp5c solution with ANN solution is observed, exhibiting the authenticity of solution methodology. Rise in the fluid transport at the center of the channel is observed with B and then turn around is evident. It may be concluded that in the middle of the channel viscous effects are negligible and maximum at the walls.

Fig. 2(b) illustrates the mean squared error (MSE) against the number of data sets through the training, validation, and testing of a model. It has been reported that the best execution achieved is 3.4803×10^{-11} at Epoch 162, as signaled by the Green Circle. The MSE reduces substantially as training progresses, presenting convergence for all datasets (train, validation, and test) around the best epoch. Fig. 2(c) showcases three subplots concluding the training procedure of a model over 162 epochs. The first subplot displays the gradient, which declines gradually, reaching 9.516×10^{-08} at epoch 162, demonstrating effective convergence. The second subplot marks the value of the parameter μ, which becomes stable at 1×10^{-10} by the final epoch, exhibiting the optimization procedure. The third subplot explains validation checks, which persist at zero all through the training, advocating no degradation in validation performance during the process. Error histogram displaying the distribution of errors for a model's predictions across three datasets: training, validation, and test is shown in Fig. 2(d). The x-axis represents the error values, while the y-axis indicates the frequency of instances in each error bin. It is reported that mostly errors are clustered around zero, representing that the model performs excellently, although there is some variance across the datasets. Fig. 2(e) represents three subplots portray the relationship between target values and model outputs for training, validation, test, and combined datasets, with all showing an R value of 1, implying accurate linear correlation. The data points are firmly aligned along with the diagonal (Y = T), exhibiting that the model's estimates closely match the targets across all datasets, indicating outstanding performance and minimal error. Fig. 2(f) gauges the function fit for output element 1. The top figure compares the model's outputs w.r.t corresponding target values, demonstrating tremendous agreement as the outputs closely aligned with the target values across the input range. The orange curve denotes the model's fit, further confirming alignment. The bottom plot explains the error, which oscillates around zero with minimal magnitude, implying that the model's predictions are highly accurate and consistent across all data splits.

Fig. 3(a) displaces the conduct of Eyring Powell material constant A, it is observed Initially that, the velocity decreases with the Eyring parameter due to surged fluid resistance from non-Newtonian effects, which suppress flow near the surface. As the Eyring parameter continues to increase, shear-thinning behavior becomes dominant, reducing viscosity and enhancing fluid motion. This leads to a rise in velocity at higher Eyring parameter values. Fig. 3(b) demonstrates the effect of velocity slip β_1, at the boundary there is rise in the velocity due to the implementation of the slip and then quatre half of the channel turnaround is visible. A slight surge in velocity is showcased in Fig. 3(c) with the electroosmotic parameter occurs initially due to enhanced electric field-driven flow near the wall. However, as the parameter increases further, ion crowding and electric double-layer effects introduce resistance, hindering the fluid motion. This leads to a reversal in the trend, causing a gradual decline in velocity. It is observed that with a -ve Helmholtz–Smoluchowski velocity parameter, the initial rise in velocity is due to enhanced electroosmotic propulsion in the direction of flow. Nonetheless, as the magnitude increases further, adverse electric field effects dominate, introducing flow resistance. This consequences in a subsequent decline in the velocity profile.

Trap bolus refers to a phenomenon where a bolus (a mass, normally fluid) trapped in a specified region due to diverse factors, for instance pressure gradients, geometrical compulsion, or other pertinent physical scenarios. In the context of biological fluid transport, a trap bolus arises in flows with complex boundary conditions, for instance in porous media, channels with hindrances. In physiological transport systems, like in the gastrointestinal tract or airways, a bolus of liquid or food, or air may trap due to motility disorders, or sphincter dysfunction. Fig. 4(a–b) show a slight decline in the size of the trapped bolus and there is small deviation in the velocity of the bolus with increase in the Eyring Powell parameter A. Rise in the size of the trapped bolus is evident from Fig. 4(b–c) as other Eyring Powell parameter B is increased. There is a substantial decline in the size of trapped bolus shown in Fig. 4(d–e) as the velocity slip is made strong.

2.3. Temperature profile

Fig. 5(a–f) showcase the analysis of ANN solution with bvp5c for temperature profile. Fig. 5(a) shows the variations of Brinkman number, there is complete unanimity of both methodologies is recorded validating the proposed solution. It has been observed that there is a substantial rise in the temperature profile, the Brinkmann number (Br) enumerates the relationship between heat generated by viscous dissipation and heat removed by thermal conduction in a fluid. Large values of Br correspond to dominance viscous forces, leading to substantial heat generation and an expansion in fluid temperature. This occurs in systems with high velocities, viscosities, or inefficient heat conduction, such as in lubrication, or microfluidics. Managing Br is fundamental to stopping overheating, which can affect system efficiency, material properties, and safety. Fig. 5(b) illustrates the MSE against the number of data sets in the process of training, validation, and testing of a model. It is worth mentioning here that the optimal execution achieved is 2.2886×10^{-13} at Epoch 42, as indicated by the Green Circle. The MSE brings down extensively as training progresses, showing convergence for all datasets around the best epoch. Fig. 5(c) stages three subplots achieving the training procedure of a model over 42 epochs. The first subplot exhibits the gradient, which drops steadily, reaching 9.9545×10^{-08} at epoch 42, establishing effective convergence. The second subplot exhibits the value of the parameter μ, which develops stable at 1×10^{-13} by the final epoch, demonstrating the optimization procedure. The third subplot describes authentication checks, which keep at zero throughout the training, raising no degradation in validation performance. Error histogram exposing the division of errors for a model's expectations across three datasets: training, validation, and test is displayed in Fig. 5(d). It is informed that most errors are assembled around zero, demonstrating that the model performs brilliantly, though there is some variation across the datasets. Fig. 5(e) symbolizes three subplots explaining the link between target values and model outputs for training, validation, test, and joint datasets, with all showing at $R = 1$, indicating accurate linear correlation. The data points are steadily allied along with the diagonal ($Y = T$), presenting that the model's approximations closely match the targets across all datasets, indicating remarkable performance and minimal error. Fig. 5(f) exposes the function fit for output element 1. The top figure assesses the model's outputs w.r.t target values, representative enormous pact as the outputs closely aligned with the target values across the input range. The underneath plot describes the error, which swings around zero, indicating that the model's predictions are greatly accurate and stable across all data sets. Fig. 6 showcase isotherm for thermal conductivity parameter α_2, thermal slip parameter β_2, and Brinkman number Br. Fig. 6(a) exhibits a decline in the temperature with an increase in the thermal conductivity parameter because higher conductivity improves heat diffusion away from the fluid. This leads to more effective thermal energy transfer, lowering the local fluid's temperature. Consequently, the overall thermal profile becomes cooler. Surge in the thermal slip parameter and electroosmotic leads to a rise in temperature (see Fig. 6(b–c)) since it lowers the heat transfer rate between the surface and fluid. This slip weakens the thermal boundary condition, allowing less heat to escape. Consequently, more heat is retained within the fluid, raising its temperature. There is decline in the temperature profile (see Fig. 6(d)) with positive value of Helmholtz Smoluchowski velocity parameter.

In the context of isotherms, the slight rise in the temperature profile witnessed in Fig. 7(a and b) for expanding α_2 signifies a gentle outward shift of isothermal lines, reflecting moderate heat retention in the fluid. In Fig. 7(c and d), the higher temperature profiles with increasing thermal slip parameter show more pronounced outward bending of isotherms. This indicates reduced thermal conduction at the surface, causing heat to accumulate near the wall and spread more broadly into the fluid. In the perspective of isotherms, the substantial expansion in the temperature profile shown in Fig. 7(e and f) with increasing Brinkmann number ($Br = 2 \rightarrow 4$) manifests intensified internal heat generation due to viscous dissipation. This outcomes in denser and more widely spaced isotherms shifting away from the surface, demonstrating elevated temperature levels throughout the fluid. The isotherms become more dispersed, illustrating a stronger thermal field influenced by higher mechanical energy conversion into heat.

2.4. Concentration profile

The impact of different flow parameters on the concentration profile are comprehensively interpreted in Fig. 8. There is moderate rise in the concentration of biofluid for rising value of Eyring Powell fluid parameter A and there is tangible inclination in the

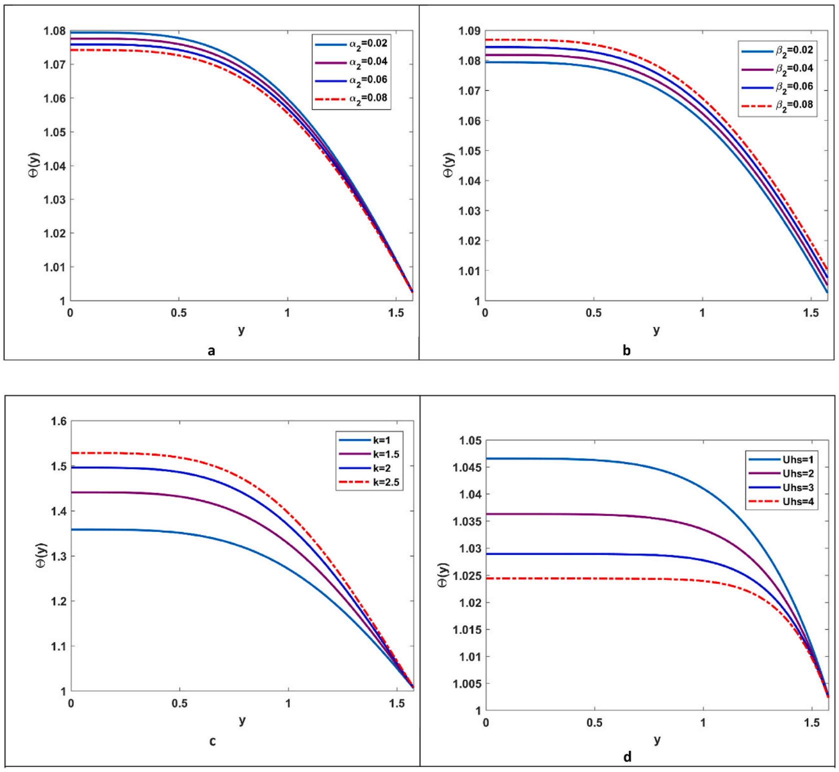

Fig. 6. The temperature profile is analyzed for different values of variable thermal conductivity, thermal slip, electroosmotic parameter and Helmholtz Smoluchowski velocity parameter with $A = 0.2, B = 0.2, m = 0.1, \alpha = 0.2; \epsilon_1 = 0.3, \epsilon_2 = 0.4, \delta = 0.01;$ $F = 2, x = 0.1, k = 1,$ $\alpha_1 = 0.02, \alpha_2 = 0.02, \beta_1 = 0.01, \beta_2 = 0.01, \beta_3 = 0.01, Sc = 0.9, Sr = 0.7, Uhs = 3.$

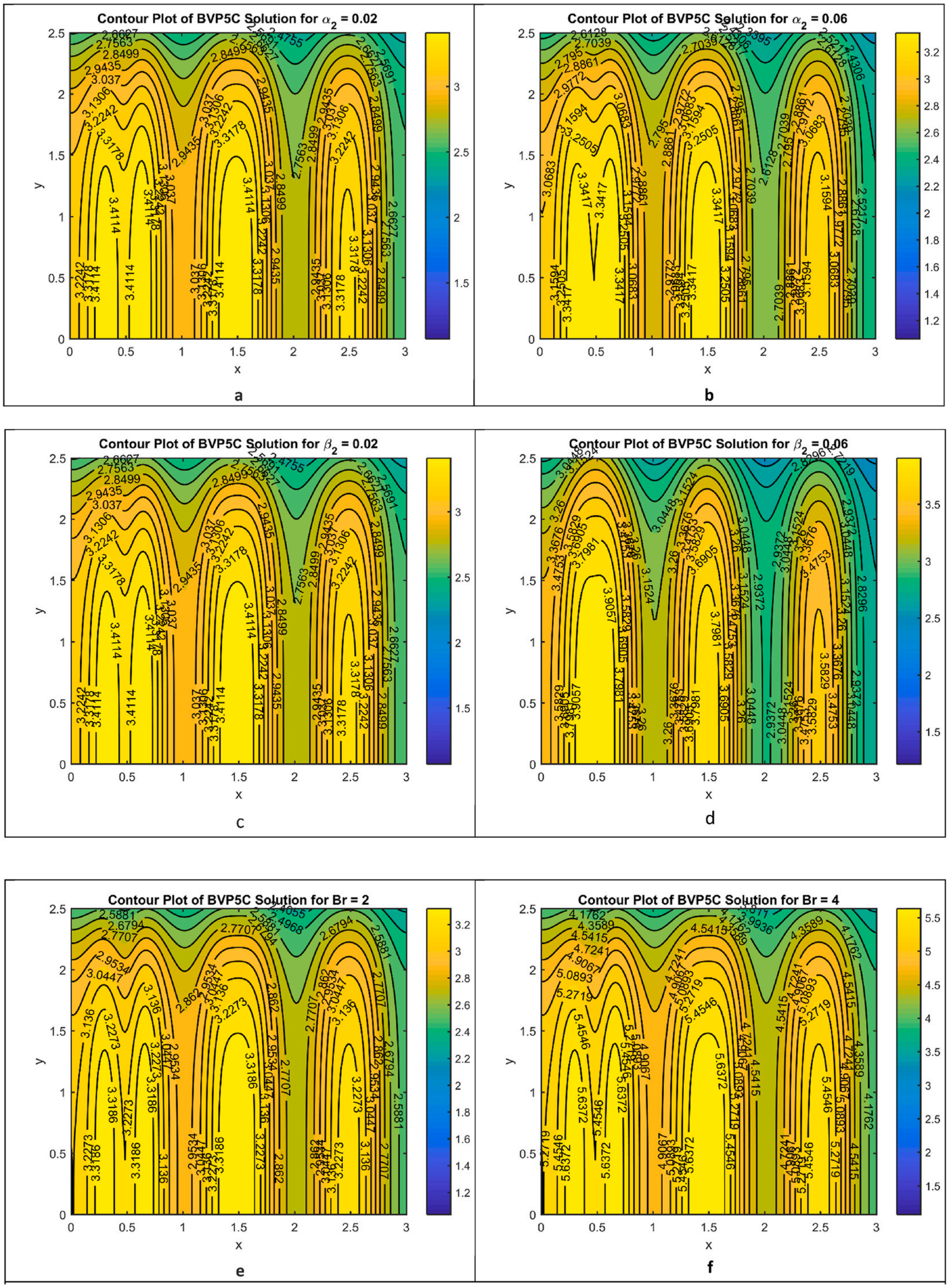

Fig. 7. Showacse isotherms plots for various values of variable thermal conductivity, thermal slip and Brikmann number with $A = 0.2$, $B = 0.2, m = 0.1, \alpha = 0.2; \epsilon_1 = 0.3, \epsilon_2 = 0.4, \delta = 0.01$; $F = 2, x = 0.1, k = 1, \alpha_1 = 0.02, \alpha_2 = 0.02, \beta_1 = 0.01, \beta_2 = 0.01, \beta_3 = 0.01, Sc = 0.9$, $Sr = 0.7, Uhs = 3$..

concentration for B see Fig. 8(a–b). There is a decline in the concentration profile observed (see Fig. 8(c)) w.r.t to concentration slip parameter β_3. The concentration slip parameter introduces a resistance at the boundary, limiting the transfer of mass between the surface and the adjacent fluid layer. Which weakened diffusion mechanism near the surface, thereby dropping the concentration gradient and overall concentration levels in the boundary layer. Physically, the slip condition reflects a scenario where the adhesion of

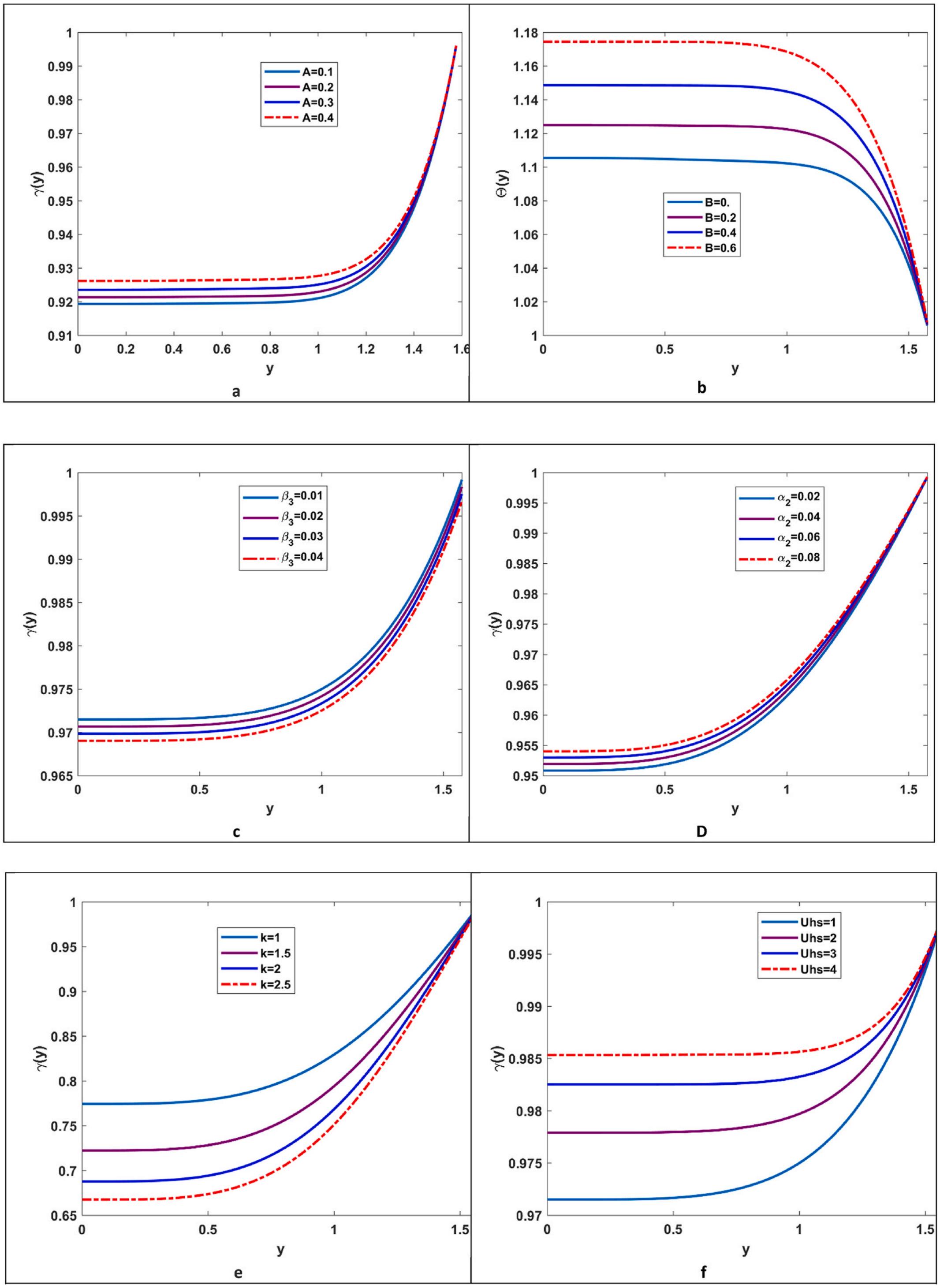

Fig. 8. Concentration profile for the variations of $A, B, \beta_3, \alpha_2, k$ and Uhs with $\boldsymbol{A} = 0.2, \boldsymbol{B} = 0.2, \boldsymbol{m} = 0.1, \boldsymbol{\alpha} = 0.2; \epsilon_1 = 0.3, \epsilon_2 = 0.4, \delta = 0.01$; $\boldsymbol{F} = 2, \boldsymbol{x} = 0.1, \boldsymbol{k} = 1, \alpha_1 = 0.02, \alpha_2 = 0.02, \beta_1 = 0.01, \beta_2 = 0.01, \beta_3 = 0.01, \boldsymbol{Sc} = 0.9, \boldsymbol{Sr} = 0.7, \boldsymbol{Uhs} = 3.$.

solute particles to the boundary is less pronounced, leading to a reduced buildup of concentration at the boundary and a consequent decline in the profile as we move away from the surface. This behavior is particularly relevant in applications involving microfluidic, or chemically reactive systems where surface effects and slip conditions portray a substantial role in transport phenomena. There is surge in diffusion phenomena of the biofluids is recorded (Fig. 8(d)) as the variable heat transfer parameter α_2 is enhanced. There is deterioration in diffusion phenomena is revealed in Fig. 8(e) as the electroosmotic parameter is enhanced. There is considerable rise in the concentration of biofluid observed as positive value of Helmholtz Smoluchowski velocity parameter is raised. The Helmholtz-Smoluchowski velocity parameter is linked with the electroosmotic flow produced due to the interaction between the electric double layer and an applied electric field. As this parameter grows positively, the electroosmotic flow becomes more prominent, driving fluid and solute particles more efficiently within the system.

2.5. Stability analysis of bvp5c solution

Fig. 9 provide Stability analysis of bvp5c solution. Fig. 9(a) depicts the stability analysis of the solution $u(y)$ attained using the BVP5C solver, where the stability measure (maximum absolute value of $u(y)$ is plotted versus the parameter B. It has been revealed that the stability measure as B increases from 0.2 to 0.8. This specifies that the solution turn into less stable (lower maximum magnitude of $u(y)$ as B increases. Such conduct recommends a sensitivity of the solution to the parameter B, expected due to its control on the boundary conditions. Fig. 9(b) establishes the stability analysis of the BVP5C solution for $\Theta(y)$, where the stability measure (maximum absolute value of $\Theta(y)$) is plotted versus the parameter β_2.As β_2 improves from 0.02 to 0.08, the stability measure show off a linear growth, implying that the solution becomes more stable with higher values of β_2 This indicates that β_2 positively affects the thermal stability of the system, likely improving the solution's robustness by modifying the thermal boundary conditions or heat transfer properties. Fig. 9(c) showacse stability analysis for γ, as the value of β_3 is increased from 0.02 to 0.08, the stability measure show off a linear growth, implying that the solution becomes more stable with higher values of β_3.

2.6. Heat and mass transfer rate

The Nusselt number (Nu) that is heat transfer rate defined as is a unitless quantity that gauges the enhancement of heat transfer within a fluid layer because of convection, compared to conduction alone. It is defined

$Nu = \frac{\partial h}{\partial x}\Theta'$ A higher Nusselt number indicates more efficient convective heat transfer relative to conduction. The bar chart (see Fig. 10(a)) illustrates the variation of the Nusselt number with different values of the Brinkman number (Br). As Br surges from 1 to 5, Nu also expands steadily, indicating boosted convective heat transfer. The trend indicates that higher viscous dissipation (represented by higher Br) results in greater thermal energy transport, as reflected by the rising Nu values. The bar chart (see Fig. 10(b)) establishes how the Nu varies with different values of the Eyring–Powell fluid parameter (B). As the value of B increases from 0.2 to 1, the Nusselt number also increases, indicating improved heat transfer. This trend recommends that higher Eyring–Powell fluid effects enhance

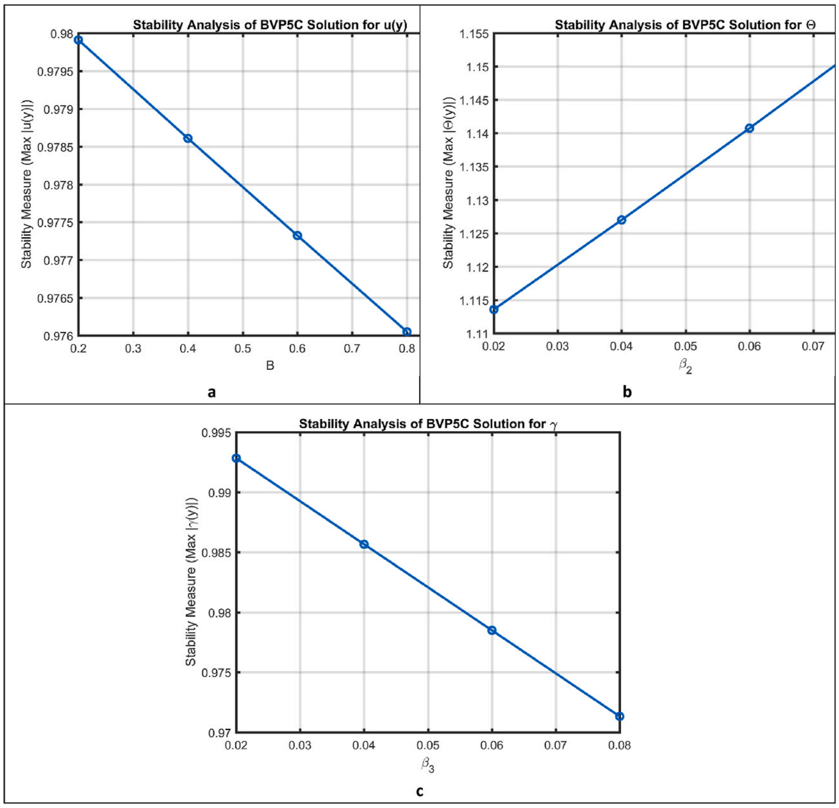

Fig. 9. Stability analysis for velocity, temperature and concentration profile.

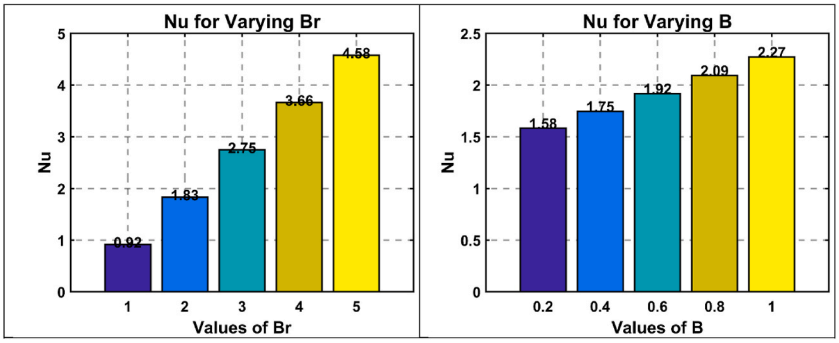

Fig. 10. Heat transfer rate as function of Br and B.

thermal conductivity, leading to more efficient convective heat transfer.

The Sherwood number (Sh) is a unitless number that represents mass transfer at a surface and is very identical to the Nusselt number. For an Eyring-Powell fluid, it's still defined traditionally as:

$$Sh = -\phi'(h).$$

The bar chart in Fig. 11(a) depicts the variation of the scaled Sherwood number with respect to the Schmidt number (Sc). As Sc increases from 0.3 to 1.2, the magnitude of $ShRe^{-0.5}$ significantly decreases, reaching its lowest at $Sc = 1.2$, before slightly increasing at $Sc = 1.5$. This trend suggests that higher Schmidt numbers initially reduce mass transfer efficiency, but beyond a certain point, the effect begins to reverse slightly. Fig. 11(b) shows how mass transfer, represented by, changes with varying concentration slip parameter β_3. As β_3 increases, the mass transfer rate initially becomes less negative, then sharply decreases around $\beta_3 = 0.02$ to 0.16, indicating a significant drop in mass transfer. This behavior suggests that higher concentration slip can initially improve mass transfer slightly, but beyond a critical point, it drastically reduces the transfer efficiency.

3. Conclusion

In this work electroosmotic based flow in a non-uniform channel carpeted with cilia for Eyring-Powell model fluid is explored. The fluid scheme is designed within a micro ciliated microchannel by implementing velocity and thermal slip boundary conditions under the influence of an electric field. Biological fluid flow is displayed employing pertinent equations of motion, which are further simplified by implementing low Reynolds number and long wavelength approximations. Solution of the physical fluid flow is supervised with bvp5c technique in MATLAB, authenticity of computation scheme is validated with ANN. The main findings of the current study may be elaborated as:

- There is an absolute alignment between the ANN and BVP5C solutions, confirming the accuracy and reliability of the proposed computational approach. This strong agreement validates the effectiveness of the neural network in approximating complex fluid behavior.
- It is observed that decline in biological fluid transport within the main flow regime under the influence of velocity slip and negative Helmholtz–Smoluchowski velocity indicates increased resistance and weakened momentum transfer near the boundary. These effects hinder fluid propulsion and reduce overall flow efficiency.

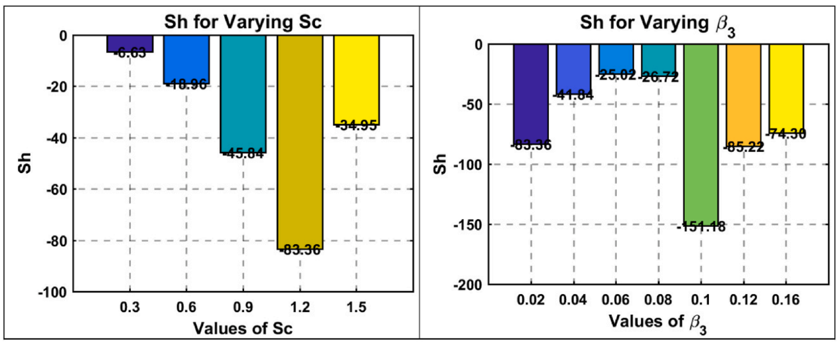

Fig. 11. Mass rate as function of Sc and β_3.

- Surge in flow due to the electroosmotic parameter highlights the significance of electrokinetic forces in enhancing fluid motion, suggesting that controlled electroosmotic effects can be strategically utilized to improve transport performance in biofluidic systems.
- Rise in biological fluid temperature with increasing Brinkmann number, thermal slip parameter, and electroosmotic parameter indicates enhanced internal heat generation, reduced surface heat exchange, and stronger electrokinetic heating effects, respectively. These factors collectively contribute to elevated thermal energy within the fluid.
- Reduction in temperature with higher thermal conductivity and Helmholtz–Smoluchowski velocity parameters demonstrates improved heat dissipation and stronger cooling effects driven by electric field-induced flow, emphasizing their roles in effective thermal regulation of biofluidic systems.
- The diffusion phenomena of biological fluid are significantly enhanced by the thermal conductivity and Helmholtz–Smoluchowski velocity parameters, as they promote better mass transport through improved thermal and electrokinetic effects.
- The diffusion phenomenon is curbed by the concentration slip parameter and electroosmotic parameter, which reduce concentration gradients and suppress solute movement near the boundary. These contrasting effects highlight the importance of carefully tuning system parameters to optimize mass transfer in biofluidic applications.
- It has been reported that the stability measure for $u(y)$ decreases as the magnetic parameter BBB increases from 0.2 to 0.8, indicated by a lower maximum magnitude of $u(y)$. This behavior suggests that the velocity profile becomes less stable under stronger magnetic influence. Such conduct highlights the sensitivity of the fluid flow solution to variations in B, emphasizing the magnetic field's significant impact on flow stability.
- As β_2 increases from 0.02 to 0.08, the stability measure exhibits a linear growth, indicating enhanced stability in the velocity profile. This trend suggests that higher values of β_2 contribute positively to the robustness of the solution, reducing sensitivity to perturbations. Thus, β_2 plays a stabilizing role in the system dynamics.

This investigation, while offering valuable understandings, the use of a simplified, symmetric microchannel geometry and a single-phase Eyring-Powell fluid model limits its applicability to more intricate physiological environments concerning multi-phase and cellular interactions. Additionally, electroosmotic effects are contemplated under ideal conditions with constant surface properties, and nonlinear or temperature-dependent slip effects are not addressed. Although the computational results are validated using ANN modeling and stability analysis, experimental validation is absent. Parametric study is also confined to specific factors, suggesting room for future work to explore broader and more dynamic conditions.

CRediT authorship contribution statement

Abaker A. Hassaballa: Writing – review & editing, Data curation, Conceptualization. **Ali Imran:** Writing – original draft, Software, Methodology, Formal analysis, Conceptualization. **Ines Hilali Jaghdam:** Visualization, Validation, Conceptualization. **Jongsuk Ro:** Supervision, Funding acquisition.

Declaration of competing interest

It is declared there is no conflict of interest involved with this work.

Acknowledgement

This work was supported by Korea Institute of Energy Technology Evaluation and Planning (KETEP) grant funded by the Korea government (MOTIE) (RS-2021-KP002504, Convergence Graduate School of Intelligent Energy and Industry. The authors extend their appreciation to Northern Border University, Saudi Arabia, for supporting this work through project number (NBU-CRP-2025-1266). Princess Nourah bint Abdulrahman University Researchers Supporting Project number (PNURSP2025R845), Princess Nourah bint Abdulrahman University, Riyadh, Saudi Arabia.

Data availability

Data will be made available on request.

References

[1] T.J. Lardner, W.J. Shack, Cilia transport, Bull. Math. Biol. 34 (1972) 325–335.
[2] A. Wanner, M. Salathé, T.G. O'Riordan, Mucociliary clearance in the airways, Am. J. Respir. Crit. Care Med. 154 (6) (1996) 1868–1902.
[3] D.J. Smith, E.A. Gaffney, J.R. Blake, Modelling mucociliary clearance, Respir. Physiol. Neurobiol. 163 (1–3) (2008) 178–188.
[4] E. Lauga, The Fluid Dynamics of Cell Motility, vol. 62, Cambridge University Press, 2020.
[5] M.C. Lagomarsino, P. Jona, B. Bassetti, Metachronal waves for deterministic switching two-state oscillators with hydrodynamic interaction, Physical Review E 68 (2) (2003) 021908.
[6] J. Elgeti, G. Gompper, Emergence of metachronal waves in cilia arrays, Proc. Natl. Acad. Sci. 110 (12) (2013) 4470–4475.
[7] R. Golestanian, J.M. Yeomans, N. Uchida, Hydrodynamic synchronization at low reynolds number, Soft Matter 7 (7) (2011) 3074–3082.
[8] N. Uchida, R. Golestanian, R.R. Bennett, Synchronization and collective dynamics of flagella and cilia as hydrodynamically coupled oscillators, J. Phys. Soc. Jpn. 86 (10) (2017) 101007.

[9] N. Muhammad, N. Ahmed, Intelligent Levenberg-Marquardt neural network solution to flow of carbon nanotubes in a nozzle of liquid rocket engine, J. Nanotechnol. 35 (2023) 85401, https://doi.org/10.1088/1361-6528/ad0e2c.
[10] T. Niedermayer, B. Eckhardt, P. Lenz, Synchronization, phase locking, and metachronal wave formation in ciliary chains, Chaos (Woodbury, N. Y.): Interdiscipl. J. Nonlinear Sci. 18 (3) (2008).
[11] A. Solovev, B.M. Friedrich, Synchronization in cilia carpets: multiple metachronal waves are stable, but one wave dominates, New J. Phys. 24 (1) (2022) 013015.
[12] Z. Asghar, K. Javid, M. Waqas, A. Ghaffari, W.A. Khan, Cilia-driven fluid flow in a curved channel: effects of complex wave and porous medium, Fluid Dyn. Res. 52 (1) (2020) 015514.
[13] J. Akram, N.S. Akbar, Electroosmotically actuated peristaltic-ciliary flow of propylene glycol+ water conveying titania nanoparticles, Sci. Rep. 13 (1) (2023) 11801.
[14] N.S. Akbar, T. Muhammad, Physical aspects of electro osmotically interactive cilia propulsion on symmetric plus asymmetric conduit flow of couple stress fluid with thermal radiation and heat transfer, Sci. Rep. 13 (1) (2023) 18491.
[15] A. Imran, M.A.Z. Raja, M. Shoaib, M. Zeb, K.S. Nisar, Electro-osmotic transport of a williamson fluid within a ciliated microchannel with heat transfer analysis, Case Stud. Therm. Eng. 45 (2023) 102904.
[16] B. Kada, A.A. Pasha, Z. Asghar, M.W.S. Khan, I.B. Aris, M.S. Shaikh, Carreau–yasuda fluid flow generated via metachronal waves of cilia in a micro-channel, Phys. Fluids 35 (1) (2023).
[17] Z. Asghar, R.A. Shah, W. Shatanawi, M.A. Gondal, M.W.S. Khan, Integrating effects of carreau–yasuda slime on bacterial hydrodynamics, Int. J. Mod. Phys. B 38 (14) (2024) 2450176.
[18] H. Sadaf, Z. Asghar, N. Iftikhar, Cilia-driven flow analysis of cross fluid model in a horizontal channel, Comput. Particle Mech. 10 (4) (2023) 943–950.
[19] K. Javid, U.F. Alqsair, M. Hassan, M.M. Bhatti, T. Ahmad, E. Bobescu, Cilia-assisted flow of viscoelastic fluid in a divergent channel under porosity effects, Biomech. Model. Mechanobiol. 20 (2021) 1399–1412.
[20] M. Ijaz Khan, A. Abbasi, S. Danish, W. Farooq, Computational analysis of cilia-mediated flow dynamics of Jeffrey nanofluid in physiologically realistic geometries, Phys. Fluids 35 (9) (2023).
[21] I.U. Rahman, M. Sulaiman, F.S. Alshammari, G. Laouini, Numerical study of nonlinear flow and mass transfer through a channel filled with a porous medium using a hybrid heuristic paradigm, Waves Random Complex Media (2023) 1–36.
[22] A. Imran, H. Alzubadi, M.R. Ali, A computation analysis with heat and mass transfer for micropolar nanofluid in ciliated microchannel: with application in the ductus efferentes, Heliyon 10 (19) (2024) e39018.
[23] A. Imran, M. Abbas, S.E. Awan, M. Shoaib, M.A.Z. Raja, Electro osmotic flow of nanofluids within a porous symmetric tapered ciliated channel, Z. Angew. Math. Mech. (2024) e202300838, https://doi.org/10.1002/zamm.202300838.
[24] P. Paul, S. Das, Electro-pumping paradigm of Non-Newtonian blood with tetra-hybrid nanoparticles infusion in a ciliated artery, Chin. J. Phys. 87 (2024) 195–231.
[25] R. Ellahi, M.M. Bhatti, K. Vafai, Effects of heat and mass transfer on peristaltic flow in a non-uniform rectangular duct, Int. J. Heat Mass Tran. 71 (2014) 706–719.
[26] S. Akram, S. Nadeem, A. Hussain, Effects of heat and mass transfer on peristaltic flow of a bingham fluid in the presence of inclined magnetic field and channel with different wave forms, J. Magn. Magn Mater. 362 (2014) 184–192.
[27] A. Rehman, M. Zeb, M.C. Khun, A. Imran, S. Ahmad, H.A. Ghazwani, Stability analysis of GO-EG and GO-blood base nanofluids by implementing of thermal radiation phenomena, Z. Angew. Math. Mech. (2024) e202300303, https://doi.org/10.1002/zamm.202300303.
[28] F.M. Allehiany, M. Alqudah, A. Imran, M.M. Alqarni, E.E. Mahmoud, A novel computational investigation for EMHD gold nanofluids in an asymmetric inclined ciliated microchannel, Ain Shams Eng. J. (2024) 102611.
[29] E.F. El-Shehawy, N.T. El-Dabe, I.M. El-Desoky, Slip effects on the peristaltic flow of a Non-Newtonian Maxwellian fluid, Acta Mech. 186 (2006) 141–159.
[30] N.M. Hafez, A.M. Abd-Alla, T.M.N. Metwaly, Influences of rotation and mass and heat transfer on MHD peristaltic transport of casson fluid through inclined plane, Alex. Eng. J. 68 (2023) 665–692.
[31] K. Saeed, S. Akram, A. Ahmad, M. Athar, A. Razia, T. Muhammad, Impact of slip boundaries on double diffusivity convection in an asymmetric channel with magneto-tangent hyperbolic nanofluid with peristaltic flow, ZAMM-Journal of Applied Mathematics and Mechanics/Zeitschrift für Angewandte Mathematik und Mechanik 103 (1) (2023) e202100338.
[32] N. Kousar, K.U. Rehman, N. Fatima, W. Shatanawi, Z. Asghar, Neural networking analysis on heat transfer in casson fluid with mixed convection equipped in staggered cavity with anti-parallel moving boundary, Int. J. Thermofluids 26 (2025) 101053.
[33] K.U. Rehman, W. Shatanawi, Z. Asghar, A.R.M. Kasim, Neural networking analysis of thermally magnetized mass transfer coefficient (MTC) for carreau fluid flow: a comparative study, Int. J. Thermofluids 26 (2025) 101069.
[34] K.U. Rehman, W. Shatanawi, L.Y. Yian, On nonlinear coupled differential system for heat transfer in magnetized enclosure with T-shaped baffle by using machine learning, Part. Differ. Equ. Applied Mathematics 13 (2025) 101078.
[35] R.E. Powell, H. Eyring, Mechanisms for the relaxation theory of viscosity, nature 154 (3909) (1944) 427–428.
[36] M. Awais, T. Salahuddin, S. Muhammad, Effects of viscous dissipation and activation energy for the MHD Eyring-powell fluid flow with darcy-forchheimer and variable fluid properties, Ain Shams Eng. J. 15 (2) (2024) 102422.
[37] M. Gudekote, R. Choudhari, P. Sanil, H. Vaidya, B. Hadimani, K.V. Prasad, J. Shetty, Impact of variable liquid properties on peristaltic transport of non-newtonian fluid through a complaint non-uniform channel, J. Adv. Res. Fluid Mech. Therm. Sci. 103 (2) (2023) 20–39.
[38] A.N. Kizhakkumpatt, G. Manjunatha, R.V. Choudhari, H. Vaidya, K.V. Prasad, K. Vajravelu, Effects of electroosmosis on peristaltic flow of eyring-powell fluid through a non-uniform channel: an application to blood flow, J. Adv. Res. Fluid Mech. Therm. Sci. 122 (2) (2024) 156–180.
[39] D. Tripathi, J. Prakash, M. Gnaneswara Reddy, R. Kumar, Numerical study of electroosmosis-induced alterations in peristaltic pumping of couple stress hybrid nanofluids through microchannel, Indian J. Phys. 95 (11) (2021) 2411–2421.
[40] V. Jagadesh, S. Sreenadh, M. Ajithkumar, P. Lakshminarayana, G. Sucharitha, Numerical exploration of the peristaltic flow of MHD Jeffrey nanofluid through a non-uniform porous channel with arrhenius activation energy, Numer. Heat Transf. A Appl. (2024) 1–15.
[41] J. Vardagala, S. Sreedharamalle, A. Moorthi, S. Gorintla, L. Pallavarapu, Hydromagnetic peristaltic flow of convective casson nanofluid through a vertical porous channel under the influence of ohmic heating and viscous dissipation effects, World J. Eng. 22 (2) (2025) 260–275.
[42] V. Jagadesh, S. Sreenadh, M. Ajithkumar, G. Sucharitha, P. Lakshminarayana, Convective peristaltic pumping of MHD Ree-Eyring nanofluid in a chemically reacting flexible divergent channel with activation energy and radiation, Radiat. Eff. Defect Solid 179 (9–10) (2024) 1162–1177.
[43] M. Ajithkumar, R. Meenakumari, G. Sucharitha, M. Vinodkumar Reddy, K. Javid, P. Lakshminarayana, Bioconvective peristaltic transport of hydromagnetic sutterby nanofluid through a chemically activated porous channel with gyrotactic microorganisms, J. Appl. Phys. 135 (19) (2024).
[44] M. Ajithkumar, P. Lakshminarayana, G. Sucharitha, K. Vajravelu, Investigation of convective peristaltic flow of Non-Newtonian fluids through a non-uniform tapered porous conduit with ohmic heating and viscous dissipation, Int. J. Model. Simulat. (2024) 1–14.
[45] Ur Rehman, W. Shatanawi, On event horizon and ergosphere of Kerr-Newman black hole: a prediction application of artificial intelligence, Int. J. Mod. Phys. D 34 (4) (2025) 2550011.
[46] K.U. Rehman, W. Shatanawi, L.Y. Yian, Neural networking-based decisions on powell–eyring fluid flow with identical stretched porous and free stream conditions, Neural Comput. Appl. (2025) 1–18.
[47] K.U. Rehman, W. Shatanawi, L.Y. Yian, AI-heat transfer analysis of casson fluid in uniformly heated enclosure with semi heated baffle, Int. J. Thermofluids 26 (2025) 101148.
[48] M. Almheidat, M. Alqudah, A. Imran, F.M. Allehiany, M.M. Alqarni, M.S. Alqurashi, E.E. Mahmoud, Thermal analysis using prandtl nanofluid in a non-uniform channel: computational paradigm focusing on complex cilia waves, Case Stud. Therm. Eng. (2025) 105872.
[49] S. Maiti, S.K. Pandey, Rheological fluid motion in tube by metachronal waves of cilia, Appl. Math. Mech. 38 (2017) 393–410.